

Study of the physical properties of Yb₂O₃-doped Gd₂Zr₂O₇ ceramics as a thermal barrier coating material

Wenxin Guo*

School of Materials Science and Engineering, North China University of Water Resources and Electric Power, 450000, PR China

Received: 7 April 2025 / Accepted: 25 October 2025

Abstract. Driven by the need for high-performance thermal barrier coatings (TBCs) in geothermal power generation, (Gd_xYb_{1-x})₂Zr₂O₇ ceramics ($x = 0.5, 0.7, 0.9, 1$) were synthesized via the solid-state reaction method. Their crystal structure (XRD), microstructure (SEM), mechanical properties (hardness, fracture toughness, Young's modulus), and thermal properties (diffusivity, conductivity) were systematically characterized to investigate the impact of Yb³⁺ doping. Major findings include: (1) All compositions exhibit a stable fluorite structure from room temperature to 873 K. (2) Yb³⁺ doping significantly reduces thermal conductivity, with the $x = 0.7$ composition achieving the minimum value of $0.858 \text{ W} \cdot \text{m}^{-1} \cdot \text{K}^{-1}$ at 675 K (>30% lower than YSZ). (3) Doping enhances hardness and fracture toughness, peaking at 10.1 GPa and $2.23 \text{ MPa} \cdot \text{m}^{1/2}$ for the $x = 0.5$ composition. (4) Young's modulus shows a non-monotonic trend with doping. This work demonstrates that Yb³⁺-doped Gd₂Zr₂O₇, particularly the $x = 0.7$ composition with ultralow thermal conductivity and sufficient mechanical strength, presents a promising candidate material for medium-high temperature (300–873 K) TBCs in geothermal applications, offering new avenues for durable coating design.

Keywords: Inorganic non-metallic materials / coating materials / thermal conductivity / hardness / toughness

1 Introduction

The global imperative for renewable energy sources has propelled geothermal power generation into prominence due to its inherent stability and environmental benefits [1]. However, a critical challenge hindering its efficiency and reliability lies in the degradation of turbine components, particularly blades and disks, which endure prolonged exposure to high-temperature steam, corrosive media, and significant thermo-mechanical stresses within geothermal systems [2,3]. Enhancing the longevity and heat resistance of these components is paramount. Thermal Barrier Coatings (TBCs) offer a vital solution by insulating metallic parts, reducing substrate temperatures, and mitigating thermal stress [4]. Consequently, the development of high-performance TBC materials exhibiting exceptional thermal insulation combined with robust mechanical integrity is crucial for advancing geothermal technology.

The current benchmark TBC material is Ytria-Stabilized Zirconia (YSZ), valued for its favorable combination of high-temperature stability, strength, toughness, low thermal conductivity (κ), and compatible thermal expansion [1]. Despite these advantages, YSZ

suffers from detrimental phase transformations above $\sim 1200^\circ\text{C}$, leading to coating failure [2,3], and faces limitations in cost-effectiveness for widespread deployment [4]. As an alternative, gadolinium zirconate (Gd₂Zr₂O₇) has garnered interest for its potential as a TBC [5]. However, its adoption is hampered by several drawbacks compared to YSZ: lower fracture toughness, rendering it more susceptible to cracking and spallation; a tendency to react with protective alumina (Al₂O₃) layers at high temperatures, forming detrimental GdAlO₃; and a relatively high coefficient of thermal expansion (CTE), exacerbating thermal mismatch stresses [5]. Recent research efforts (e.g., [6–8]) have explored various doping strategies to improve specific properties of zirconates, such as further reducing κ or enhancing phase stability.

While progress has been made, a significant gap remains: most existing studies focus primarily on optimizing *single* properties (e.g., minimizing κ or improving toughness). There is a pressing need for novel TBC materials, especially for medium-high temperature (e.g., 300–873 K) geothermal applications, that simultaneously achieve ultra-low thermal conductivity and enhanced mechanical properties (notably hardness and fracture toughness) to ensure both effective thermal insulation and resistance to impact damage and thermal cycling stresses. Achieving this dual-property optimization represents a key opportunity for advancement.

* e-mail: gwenxinguo@outlook.com

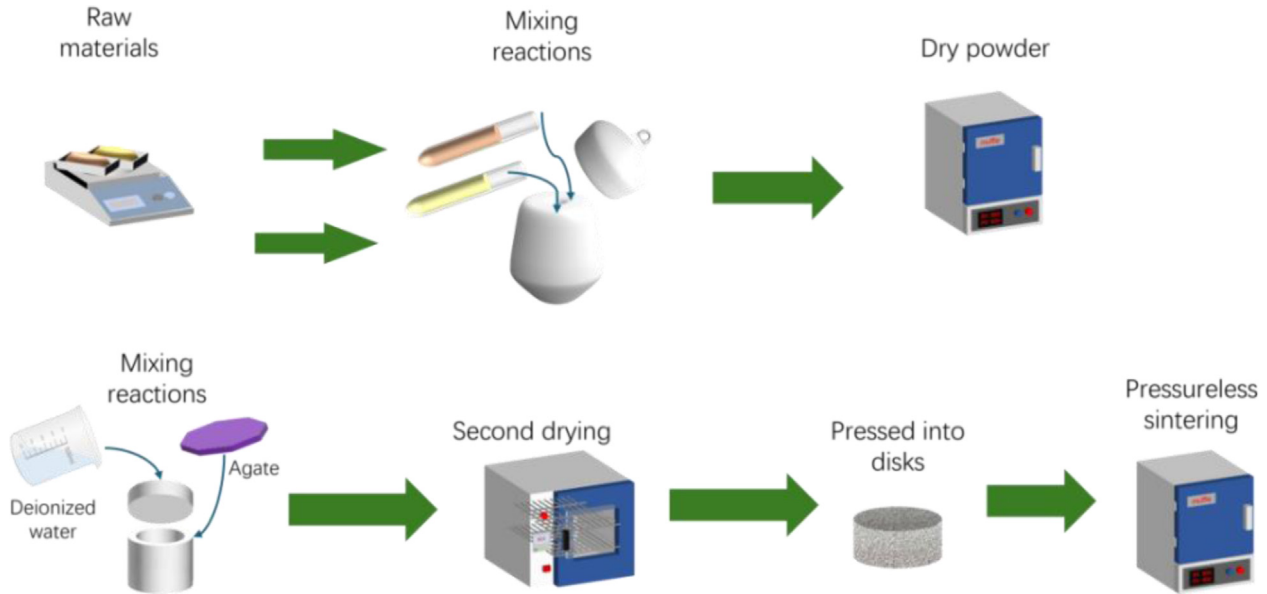


Fig. 1. Sample preparation flow chart.

To bridge this gap, this study proposes doping Yb^{3+} (using Yb_2O_3) into the $\text{Gd}_2\text{Zr}_2\text{O}_7$ lattice to form $(\text{Gd}_x\text{Yb}_{1-x})_2\text{Zr}_2\text{O}_7$ ceramics ($x=0.5, 0.7, 0.9, 1$). These materials were synthesized via the solid-state reaction method. A comprehensive characterization was undertaken to systematically evaluate the impact of Yb^{3+} doping on: crystal structure and phase stability (using X-ray Diffraction – XRD), microstructure (using Scanning Electron Microscopy – SEM), mechanical properties (Vickers hardness, fracture toughness, Young’s modulus), and thermal properties (thermal diffusivity and derived thermal conductivity). The primary goal is to elucidate the structure-property relationships and identify compositions offering an optimal balance of low κ and enhanced mechanical performance.

The key findings and contributions of this work are:

- Successful synthesis of $(\text{Gd}_x\text{Yb}_{1-x})_2\text{Zr}_2\text{O}_7$ ceramics exhibiting a stable fluorite structure across the temperature range of interest (room temperature to 873 K).
- Demonstration that Yb^{3+} doping significantly reduces thermal conductivity, with the $x=0.7$ composition achieving a minimum κ of $0.858 \text{ W} \cdot \text{m}^{-1} \cdot \text{K}^{-1}$ at 675 K (representing a $>30\%$ reduction compared to YSZ).
- Evidence that Yb^{3+} doping enhances hardness and fracture toughness, reaching peak values of 10.1 GPa and $2.23 \text{ MPa} \cdot \text{m}^{1/2}$, respectively, for the $x=0.5$ composition.
- Insights into the underlying mechanisms, linking Yb^{3+} doping to lattice distortion, phonon scattering (reducing κ), and grain refinement/dislocation pinning (enhancing mechanical properties).
- Identification of the $(\text{Gd}_{0.7}\text{Yb}_{0.3})_2\text{Zr}_2\text{O}_7$ composition as a highly promising candidate material for thermal barrier coatings in geothermal turbine applications, offering an exceptional combination of ultralow thermal conductivity and sufficient mechanical strength within the target temperature range.

The remainder of this paper is structured as follows: Section 2 details the sample preparation (solid-state reaction) and testing methodologies (XRD, SEM, mechanical testing, thermal diffusivity/conductivity measurement). Section 3 presents and discusses the results, covering phase structure (3.1), microstructure (3.2), mechanical properties (3.3), and thermal properties (3.4). Finally, Section 4 summarizes the key conclusions.

Compared with recent literature (e.g., [6–8]), it is pointed out that most existing studies focus on single-property optimization, while this study achieves a balance between thermal conductivity and mechanical properties through Yb^{3+} doping.

2 Sample preparation and testing

2.1 Sample preparation

This section details the solid-state reaction protocol for synthesizing $(\text{Gd}_x\text{Yb}_{1-x})_2\text{Zr}_2\text{O}_7$ ceramics, encompassing raw material stoichiometry, ball milling parameters, sintering conditions, and density characterization, providing the methodological basis for material performance evaluation.

In the sample preparation process, as illustrated in Figure 1, the first step is to weigh the corresponding oxide raw materials according to their stoichiometric ratios. Subsequently, the raw powder is placed in a muffle furnace at 120°C for 2 h for drying to eliminate adsorbed moisture and some volatile organic impurities that may have been introduced during storage and weighing, thereby enhancing the material’s purity. Following drying, the powder is transferred into a ball milling jar, where deionized water and agate balls are added for ball milling and mixing, ensuring a homogeneous mixture and initiating a preliminary reaction. The ball – milled powder is then dried again at 120°C to further remove moisture and volatile

compounds. Once drying is complete, the powder undergoes pressing to form pellets under a pressure of 5 MPa. The pressed samples are then sintered in a muffle furnace at 1550 °C for 10 h under no applied pressure. After sintering, the bulk samples are subjected to density measurements using Archimedes' drainage method. Finally, the densified bulk material is selected for X-ray characterization.

2.2 Sample testing

Herein, the characterization techniques for crystal structure (XRD), microstructure (SEM), mechanical properties (Young's modulus, hardness, fracture toughness), and thermal properties (diffusivity, conductivity) are systematically described, enabling comprehensive analysis of Yb³⁺ doping effects on material behavior.

X-ray Diffraction (XRD): The crystal structure and phase composition of the samples prepared via the solid – state method are analyzed using a D8 Advance X – ray diffractometer with Cu K α radiation ($\lambda = 0.15406$ nm). The scanning rate is set at 2 min per scan, with a step size of 0.01° and a scanning range of 20° to 70°. Detailed lattice parameters of the material can be derived through XRD refinement. The equation $2d \sin \theta = n\lambda$ is used to assist in the analysis of the crystal structure characteristics. The identification of the crystal structure is based on the comparison with the standard pattern from the ICDD database. **Scanning Electron Microscopy (SEM):** Scanning electron microscopy is employed to examine the grain size and morphology of the samples. Since the samples are insulating, gold sputtering is performed to ensure effective analysis.

Young's Modulus: The longitudinal and transverse sound velocities of the material are measured using the ultrasonic reflection technique. The Young's modulus is then calculated using the appropriate formula

$$E_0 = \frac{E(\varphi)}{\left(1 - \varphi^{\frac{2}{3}}\right)^{1.21}} \quad (1)$$

$$G = \frac{E_0}{2(1 + \nu)} \quad (2)$$

and complementary formulas, used for calculating the mechanical property parameters such as Young's modulus, bulk modulus, and shear modulus of materials.

E_0 : Young's modulus

$E(\varphi)$: Young's modulus value related to porosity

G : Shear modulus

φ : Porosity

ν : Poisson's ratio

$$E_{corr} = E_0 \times \left(1 - \alpha \cdot \frac{k}{k_0}\right) \quad (3)$$

where E_{corr} is the corrected Young's modulus, E_0 is the raw measured Young's modulus, α is a material-specific correction coefficient (determined to be 0.02 in this study),

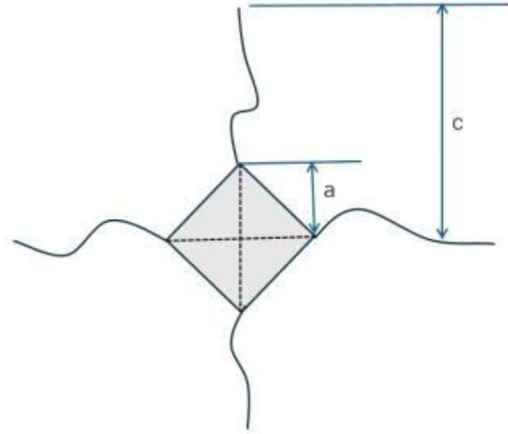


Fig. 2. Figure note: Vickers hardness.

k is the thermal conductivity of the sample, and k_0 is the reference thermal conductivity at room temperature ($1.2 \text{ W} \cdot \text{m}^{-1} \cdot \text{K}^{-1}$).

Hardness and Fracture Toughness: The hardness and fracture toughness of the material were tested using an automated micro-Vickers hardness tester, and the fracture toughness was measured using the indentation method, as shown schematically in Figure 2, where there is a link between the crack length, c , and the fracture toughness, K_{IC} , as follows.

$$K_{IC} = \beta \left(\frac{E}{H}\right)^{1/2} \left(\frac{P}{c^{3/2}}\right) \quad (4)$$

where β is an empirical constant related to the geometry of the indenter. For an indenter with a square cross-section, $\alpha = 0.018$. Here, P represents the applied load (500 g in the experiment), E is Young's modulus, H is hardness, and c is the crack length. Five different positions on each sample were selected for Vickers hardness testing with a load of 500 g and a dwell time of 10 s, and the average value and standard deviation were calculated; fracture toughness was measured by the 9-point indentation method with an error range controlled within $\pm 5\%$.

Thermal Diffusivity Testing: The thermal diffusivity coefficient α is a key parameter in determining a material's thermal conductivity. It was measured using a laser thermal conductivity apparatus. The sample used for testing was a circular disc with a diameter of 12.8 mm and a thickness of 1.2 mm. The experiment was conducted under a high-purity argon atmosphere, with a heating rate ranging from 1 °C to 8 °C per minute. As the test temperature increased, the heating rate also escalated. After performing three measurements at each temperature point, the average value was taken to calculate the thermal conductivity. Thermal conductivity quantifies a material's ability to conduct heat. It is influenced by factors such as the material's density, porosity, and specific heat capacity. The relationship is expressed by the formula:

$$K' = \rho \cdot \lambda \cdot C_p \quad (5)$$

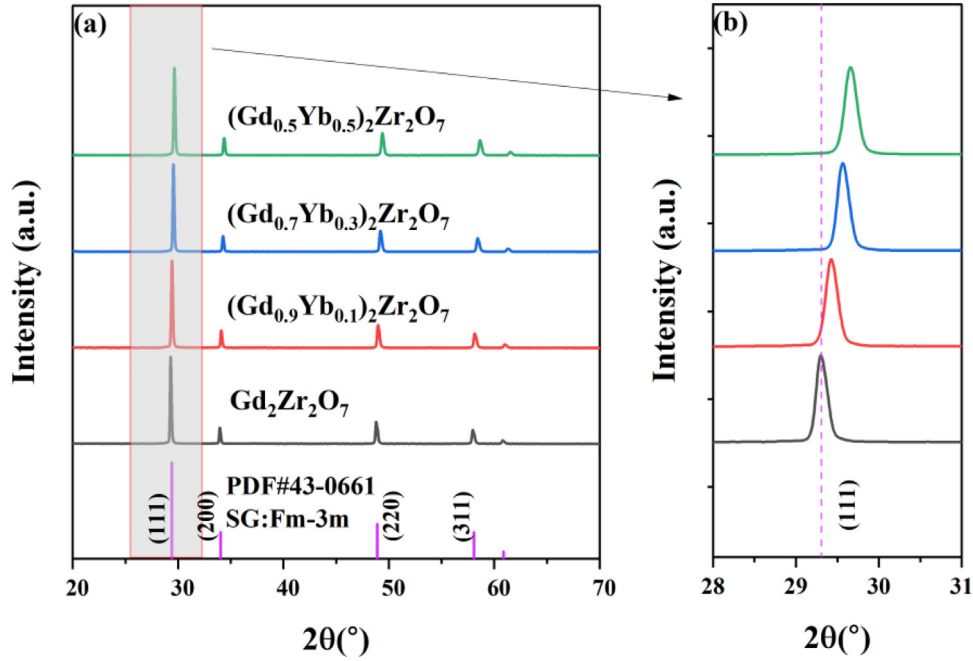


Fig. 3. XRD pattern of $(\text{Gd}_x\text{Yb}_{1-x})_2\text{Zr}_2\text{O}_7$.

where K' is the thermal conductivity, λ is the thermal diffusivity, C_P is the specific heat capacity, and ρ is the density [9]. This formula is derived from Fourier's law of heat conduction and is applicable to calculating the thermal conductivity of homogeneous and isotropic materials under steady-state heat conduction conditions. In this study, the $(\text{Gd}_x\text{Yb}_{1-x})_2\text{Zr}_2\text{O}_7$ ceramic materials can be approximately considered to meet the above-mentioned conditions within the experimental measurement temperature range. Therefore, this formula is used to calculate the thermal conductivity. Density and porosity can be calculated using the following formulas:

$$\rho = \frac{m_1}{(m_3 - m_2)} \quad (6)$$

and

$$\varphi = 1 - \frac{\rho}{\rho_0} \quad (7)$$

Where ρ is the actual density of the ceramic material, measured using the drainage method based on Archimedes' principle.

m_1 : Mass of the sample in air

m_2 : Apparent mass of the sample when it is completely immersed in water

m_3 : Mass of the sample after saturated water absorption

The theoretical density ρ_0 is given by:

$$\rho_0 = \frac{W}{V} \quad (8)$$

W: mass V: volume

The specific heat capacity C_p is determined using the Neumann-Kopp law.

Specifically, the heat capacities of the constituent oxides are obtained from thermodynamic reference tables [10], and the material's specific heat capacity is then calculated by a weighted average based on the mass fraction of each oxide. Preliminary results indicate that the error between the specific heat capacity calculated using the Neumann-Kopp law and the values obtained from differential thermal analysis is less than 2%. Thus, this study uses the specific heat capacity value calculated by the Neumann-Kopp law.

3 Results and discussion

3.1 Phase structure

This section presents XRD analysis results of $(\text{Gd}_x\text{Yb}_{1-x})_2\text{Zr}_2\text{O}_7$ ceramics, discussing phase composition, lattice parameter variations, and structural transitions induced by Yb^{3+} doping, which underpin the understanding of thermal and mechanical property mechanisms.

Figure 3 presents the X-ray diffraction (XRD) patterns of $(\text{Gd}_x\text{Yb}_{1-x})_2\text{Zr}_2\text{O}_7$ ceramic materials with $x=0.5, 0.7, 0.9,$ and 1 .

As shown in Figure 3, the $(\text{Gd}_{0.9}\text{Yb}_{0.1})_2\text{Zr}_2\text{O}_7$, and $\text{Gd}_2\text{Zr}_2\text{O}_7$ samples, synthesized using the solid-state method, are single-phase materials. From the XRD patterns, characteristic peaks at $28^\circ, 33^\circ, 47^\circ,$ and 56° are observed, corresponding to the (111), (200), (220), and (311) planes, respectively. These peaks align with the standard fluorite structure's characteristic reflections [11], indicating that the synthesized ceramic materials adopt the fluorite structure. In other studies [12], it has been found that when other elements are doped into fluorite, the

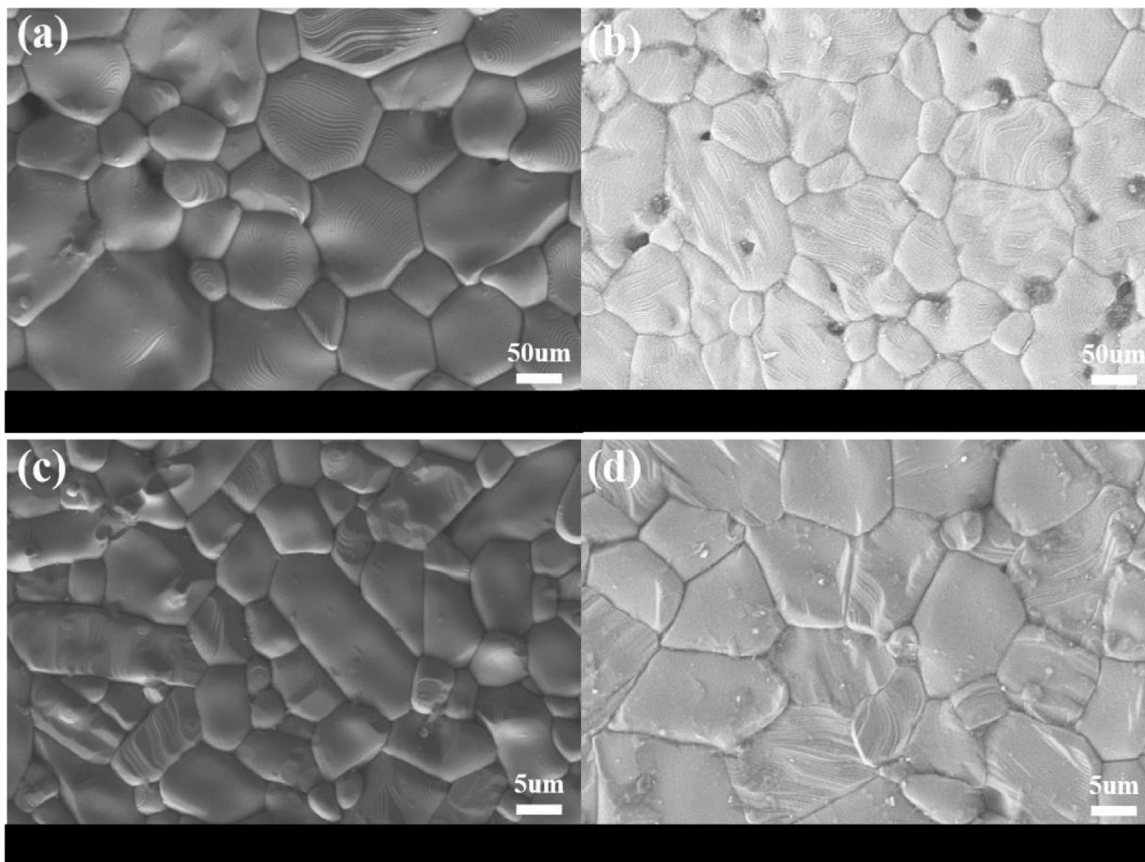


Fig. 4. SEM photographs of $(\text{Gd}_x\text{Yb}_{1-x})_2\text{Zr}_2\text{O}_7$ ceramic surface. a) $\text{Gd}_2\text{Zr}_2\text{O}_7$, b) $(\text{Gd}_{0.9}\text{Yb}_{0.1})_2\text{Zr}_2\text{O}_7$, c) $(\text{Gd}_{0.7}\text{Yb}_{0.3})_2\text{Zr}_2\text{O}_7$, d) $(\text{Gd}_{0.5}\text{Yb}_{0.5})_2\text{Zr}_2\text{O}_7$.

structure transforms into a pyrochlore structure, resulting in an ordered – disordered transition [13]. The primary reason for this transformation is the increase in the atomic radius ratio between the A – site and B – site ions. For larger radius ratios, the ordered arrangement of A and B ions lowers the system's energy, stabilizing the structure and resulting in the formation of the ordered pyrochlore structure. In contrast, when the radius ratio is smaller, the A and B ions have similar radii, leading to a disordered arrangement and the formation of the fluorite structure.

The crystal structure of $\text{A}_2\text{B}_2\text{O}_7$ -type ceramic materials is primarily determined by the ratio of the A-site ion radius to the B-site ion radius [14]. When this ratio falls between 1.46 and 1.78, the material forms a cubic pyrochlore structure. However, when the ratio is below 1.46, the material adopts a defective fluorite structure [15].

It can also be seen from the XRD patterns that varying doping levels cause different degrees of peak shifts. When Yb^{3+} partially replaces Gd^{3+} at the A-site, the diffraction peaks shift to higher angles. The magnitude of the shift increases with the doping concentration. This shift occurs because the substitution of atoms with different ionic radii leads to changes in the unit cell volume [16,17]. The smaller Yb^{3+} ion reduces the interplanar spacing, increasing the diffraction angle. According to Bragg's law, this causes a corresponding shift in the diffraction peak positions.

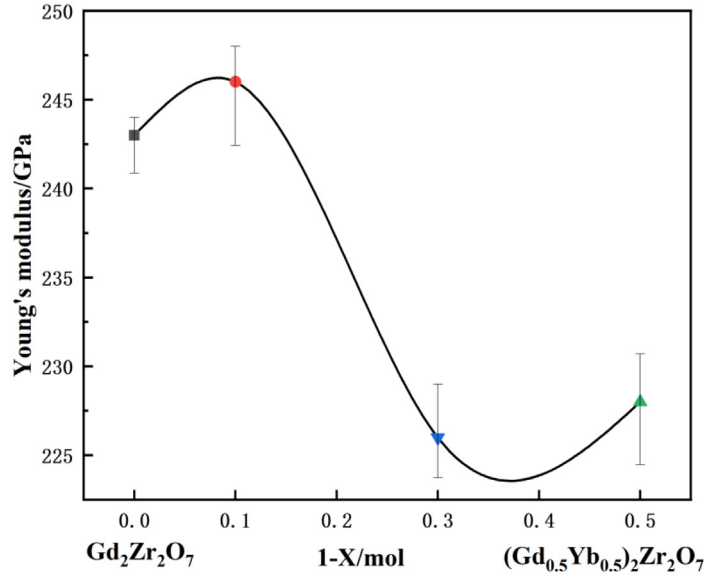
Microstructural analysis further reveals the effect of doping on grain growth.

3.2 Microstructure

Figure 4 presents the surface morphology of the $(\text{Gd}_x\text{Yb}_{1-x})_2\text{Zr}_2\text{O}_7$ system with different compositions after heat treatment at 1550°C for 10 h. As shown in Figure 4, the single-phase compositions ($x=1.0$ and $x=0.9$) exhibit an average grain size of $\sim 50\ \mu\text{m}$. In contrast, the dual-phase compositions ($x=0.7$ and $x=0.5$) show significant grain refinement ($\sim 1.5\ \mu\text{m}$). The two phases are Yb-rich fluorite (EDS: 28.5 Gd, 15.2 Yb, 56.3 Zr at%) and Gd-rich pyrochlore (EDS: 31.8 Gd, 5.1 Yb, 63.1 Zr at%). The grain refinement effect observed in these samples is attributed to the mutual inhibition between the two phases during grain growth. The difficulty in mass transfer between the two phases during heat treatment leads to competition and inhibition, limiting grain growth [18,19].

3.3 Mechanical property

The mechanical performance of $(\text{Gd}_x\text{Yb}_{1-x})_2\text{Zr}_2\text{O}_7$ ceramics, including Young's modulus, Vickers hardness, and fracture toughness, is evaluated in this section. The discussion focuses on how Yb^{3+} doping enhances mechanical properties via lattice distortion and grain boundary strengthening mechanisms.



Horizontal axis: "1-x (molar fraction of Yb_2O_3 doping)"; Vertical axis: "Young's modulus (GPa)".

■ $x=1$, ● $x=0.9$, ▼ $x=0.7$, ▲ $x=0.5$

Fig. 5. Young's modulus of $(\text{Gd}_x\text{Yb}_{1-x})_2\text{Zr}_2\text{O}_7$. (Error range: within $\pm 5\%$).

When studying the mechanical properties of materials, there is a certain correlation between thermal conductivity and Young's modulus. The change in thermal conductivity will affect the energy transfer within the material, which in turn acts on the lattice vibration. Lattice vibration is closely related to the elastic properties of the material, and Young's modulus is one of the important indicators of the elastic properties of the material. Therefore, when analyzing the changes in Young's modulus, the influence of thermal conductivity needs to be taken into account.

The Young's modulus of the sample system was measured using the ultrasonic reflection method, and the influence of thermal conductivity was corrected using a formula, as shown in Figure 5.

It can be seen from Figure 5 that as the thermal conductivity changes, the Young's modulus also shows corresponding changes. When the thermal conductivity is low, for example, in the $(\text{Gd}_{0.5}\text{Yb}_{0.5})_2\text{Zr}_2\text{O}_7$ sample, its Young's modulus is relatively low. This is because a low thermal conductivity means that the energy transfer efficiency of lattice vibration within the material is low. The amplitude and frequency of lattice vibration are affected, which weakens the elastic recovery ability of the lattice, thus leading to a decrease in the Young's modulus. On the contrary, for samples with higher thermal conductivity, such as $(\text{Gd}_{0.9}\text{Yb}_{0.1})_2\text{Zr}_2\text{O}_7$, their Young's modulus is relatively high, indicating that when the energy transfer of lattice vibration is better, the elasticity of the lattice can be maintained better, thereby increasing the Young's modulus.

As shown in Figure 5, Young's modulus of the single-phase solid solution is similar to that of the matrix composition, while Young's modulus of the mixed

compositions is lower than that of the single-phase materials. This may be due to the relatively weaker boundary strength in the mixture [20].

The reversal of Young's modulus and hardness trends in the $(\text{Gd}_x\text{Yb}_{1-x})_2\text{Zr}_2\text{O}_7$ system is primarily attributed to the mixed-phase structure. In mixed-phase materials, smaller grain sizes and grain boundary strengthening impede dislocation motion, enhancing hardness. Conversely, Young's modulus is influenced by lattice softening induced by point defects (e.g., Yb^{3+} substitution), which reduces the elastic recovery capacity of the lattice, leading to a decrease in modulus despite increased hardness.

In solid solutions, the stress field induced by point defects can alter the material's elastic properties, thereby affecting the transmission of lattice vibrational energy [21]. Solute atoms in interstitial positions contribute to matrix hardening, while the effects of substitutional atoms on the elastic properties are less well understood. In the study by Ibegazene et al., the substitution of ZrO_2 with HfO_2 in YSZ led to a significant increase in Young's modulus, primarily due to the formation of a new phase. However, no new phase was formed in the present sample system, and it is observed that Young's modulus of the solid solution components is lower than the linear mixing values of the single-phase materials. Therefore, it can be inferred that in this sample system, the differences in size and interaction forces between the substituent atoms and the surrounding matrix lead to lattice "softening," and the stress field caused by point defects induce lattice relaxation [6]. Lattice relaxation results in reduced phonon velocity, which in turn lowers thermal conductivity. Consequently, the lower Young's modulus leads to reduced thermal conductivity. Moreover, for coating materials, a low Young's modulus

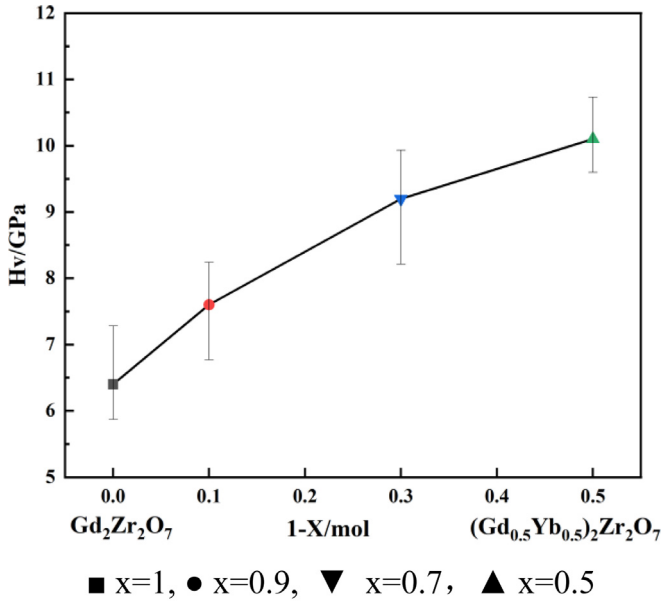


Fig. 6. Hardness of $(\text{Gd}_x\text{Yb}_{1-x})_2\text{Zr}_2\text{O}_7$. (Error range: within $\pm 5\%$).

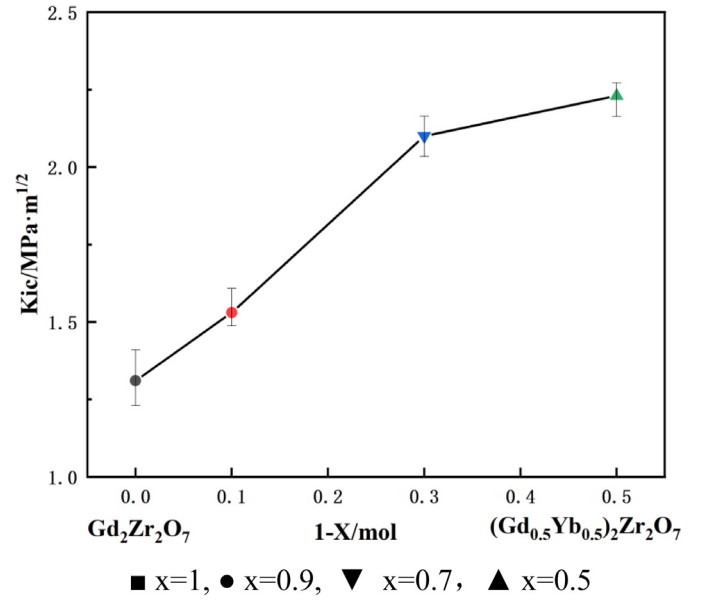


Fig. 7. Fracture toughness of $(\text{Gd}_x\text{Yb}_{1-x})_2\text{Zr}_2\text{O}_7$. (Error range: within $\pm 5\%$).

is highly advantageous, as it helps reduce thermal stress during heating and cooling cycles due to thermal mismatch, thereby enhancing the stability and lifespan of the coating [7].

In this study, the Vickers hardness of the samples was measured using the indentation method. The results of these measurements are shown in Figure 6. As depicted in Figure 6, the hardness of $(\text{Gd}_{0.9}\text{Yb}_{0.1})_2\text{Zr}_2\text{O}_7$, $(\text{Gd}_{0.7}\text{Yb}_{0.3})_2\text{Zr}_2\text{O}_7$, and $(\text{Gd}_{0.5}\text{Yb}_{0.5})_2\text{Zr}_2\text{O}_7$ is higher than that of $\text{Gd}_2\text{Zr}_2\text{O}_7$, which is inconsistent with the trend observed for Young's modulus. As shown in Figure 6, the hardness of $(\text{Gd}_{0.9}\text{Yb}_{0.1})_2\text{Zr}_2\text{O}_7$, $(\text{Gd}_{0.7}\text{Yb}_{0.3})_2\text{Zr}_2\text{O}_7$, and $(\text{Gd}_{0.5}\text{Yb}_{0.5})_2\text{Zr}_2\text{O}_7$ is 15–30% higher than that of $\text{Gd}_2\text{Zr}_2\text{O}_7$ (6.8 GPa). Compared with the traditional thermal barrier coating material YSZ (hardness ~ 8.5 GPa, fracture toughness $\sim 1.8 \text{ MPa}\cdot\text{m}^{1/2}$) [1,2], the $(\text{Gd}_{0.5}\text{Yb}_{0.5})_2\text{Zr}_2\text{O}_7$ ceramic exhibits superior hardness (10.1 GPa) and fracture toughness ($2.23 \text{ MPa}\cdot\text{m}^{1/2}$), as shown in Figure 7. This improvement is attributed to Yb^{3+} -induced grain refinement (SEM observations in Figure 4 show grain size reduced from $50 \mu\text{m}$ to $1.5 \mu\text{m}$) and lattice distortion, which enhance dislocation pinning at grain boundaries and improve impact resistance. Generally, a lower Young's modulus correlates with lower hardness. However, in the $(\text{Gd}_x\text{Yb}_{1-x})_2\text{Zr}_2\text{O}_7$ system, this trend is reversed, primarily due to the mixed-phase composition [8].

When measuring hardness using the indentation method, plastic deformation occurs in the material, with dislocation generation and movement being the primary mechanisms. In the mixed-phase system, smaller grain sizes cause grain boundaries to impede dislocation motion, thereby reducing plastic deformation and increasing hardness.

The fracture toughness of the samples was measured using the cracks generated during the Vickers hardness test, and the calculated fracture toughness values are presented in the figure below.

From the figure, it can be observed that the fracture toughness of the mixed-phase compositions is higher than that of the single-phase compositions. Among the single-phase compositions, the fracture toughness of the solid solutions is slightly higher than that of the matrix composition. As the Yb^{3+} doping amount increases, both the hardness and fracture toughness of the ceramic materials increase, indicating that Yb^{3+} doping improves their mechanical properties. When $x=0.5$, the hardness and fracture toughness of $(\text{Gd}_x\text{Yb}_{1-x})_2\text{Zr}_2\text{O}_7$ ceramic materials reach their maximum values of 10.1 (Hv/GPa) and $2.23 \text{ (Kic/MPa}\cdot\text{m}^{1/2})$, respectively.

The smaller ionic radius of the doped Yb^{3+} reduces the average distance between ions, leading to an increase in lattice energy. Lattice energy is the energy required to separate a unit amount of an ionic crystal, and the larger the lattice energy, the more stable the crystal. As a result, the hardness and fracture toughness of the crystal are enhanced because more energy is required to break the crystal [22]. Therefore, doping with Yb^{3+} improves the hardness and fracture toughness of the material.

Fracture toughness has now become one of the key indicators for coating materials. Gas turbines equipped with coatings are subject to impacts from foreign objects during high-speed operation, making the toughness of the coating material crucial. High-toughness materials can reduce crack propagation and minimize damage caused by collisions [23]. In the samples, the fracture toughness of the fine-grained biphasic composite compositions is significantly higher than that of the single-phase composition. This mechanism is primarily related to the microstructure, and the fracture toughness measured by the indentation method reflects crack propagation behavior. As shown in the figure, the maximum fracture toughness value is $2.23 \text{ MPa}\cdot\text{m}^{1/2}$, which represents a clear improvement compared to the single-phase $\text{Gd}_2\text{Zr}_2\text{O}_7$ and shows promise as a potential candidate for coating materials.

3.4 Thermal properties

Thermal diffusivity and conductivity data of the ceramics across 300–900 K are presented herein, elucidating the influence of Yb^{3+} -induced point defects and lattice anharmonicity on heat transport, which is critical for thermal barrier coating applications.

The thermal diffusivity of the samples was measured using laser scattering, as shown in Figure 8.

It can first be observed that with the increase in temperature, the thermal diffusivity of the four ceramic compositions exhibits a downward trend. At the same temperature, the thermal diffusivity of $(\text{Gd}_{0.9}\text{Yb}_{0.1})_2\text{Zr}_2\text{O}_7$ is greater than that of $\text{Gd}_2\text{Zr}_2\text{O}_7$, which is greater than $(\text{Gd}_{0.5}\text{Yb}_{0.5})_2\text{Zr}_2\text{O}_7$, and the thermal diffusivity of $(\text{Gd}_{0.7}\text{Yb}_{0.3})_2\text{Zr}_2\text{O}_7$ is the lowest. At 873 K, the thermal diffusivity of $(\text{Gd}_x\text{Yb}_{1-x})_2\text{Zr}_2\text{O}_7$ with $x=0.7$ reaches the lowest value of $0.326 \text{ mm}^2/\text{s}$.

At different temperatures, the thermal diffusivity of $(\text{Gd}_{0.9}\text{Yb}_{0.1})_2\text{Zr}_2\text{O}_7$ is consistently higher than that of $(\text{Gd}_{0.7}\text{Yb}_{0.3})_2\text{Zr}_2\text{O}_7$. From the previous discussion, it is known that $(\text{Gd}_{0.9}\text{Yb}_{0.1})_2\text{Zr}_2\text{O}_7$ and $(\text{Gd}_{0.7}\text{Yb}_{0.3})_2\text{Zr}_2\text{O}_7$ have the same concentration of oxygen vacancies, so the contribution of defect scattering to the phonon mean free path should be similar. The lower thermal diffusivity of $(\text{Gd}_{0.7}\text{Yb}_{0.3})_2\text{Zr}_2\text{O}_7$ versus $(\text{Gd}_{0.9}\text{Yb}_{0.1})_2\text{Zr}_2\text{O}_7$ (Fig. 8) suggests stronger phonon scattering, likely due to enhanced lattice anharmonicity induced by Yb^{3+} doping. This is supported by the greater lattice distortion observed in XRD peak broadening (FWHM increased by 18% at $x=0.3$ vs $x=0.1$, Fig. 3) and reduced Young's modulus (Fig. 5). While CTE data would strengthen the anharmonicity analysis, current evidence from lattice distortion and elastic properties consistently points to Yb^{3+} -enhanced phonon scattering. As a result, phonon scattering in $(\text{Gd}_{0.9}\text{Yb}_{0.1})_2\text{Zr}_2\text{O}_7$ is weaker, leading to a longer phonon mean free path and higher thermal diffusivity compared to $(\text{Gd}_{0.7}\text{Yb}_{0.3})_2\text{Zr}_2\text{O}_7$ [24].

At low temperatures, the thermal diffusivity of $(\text{Gd}_{0.7}\text{Yb}_{0.3})_2\text{Zr}_2\text{O}_7$ and $(\text{Gd}_{0.5}\text{Yb}_{0.5})_2\text{Zr}_2\text{O}_7$ is significantly lower than that of the matrix composition. The sharp change between them is mainly due to the difference in the concentration of point defects, which leads to different degrees of phonon scattering. The higher concentration of point defects in $(\text{Gd}_{0.7}\text{Yb}_{0.3})_2\text{Zr}_2\text{O}_7$ and $(\text{Gd}_{0.5}\text{Yb}_{0.5})_2\text{Zr}_2\text{O}_7$ compared to the matrix composition results in stronger phonon scattering and a lower thermal diffusivity. This is mainly due to the strong scattering effect of point defects on phonons. It can also be observed that at the same temperature, the transition in thermal diffusivity between the single-phase solid solution and mixed-phase compositions is continuous, with no obvious abrupt change, indicating that the interfaces introduced by the two-phase mixing have minimal effect on phonon scattering.

Specific heat is also a factor influencing thermal conductivity because it determines the capacity of phonons to carry energy during their motion. To date, there has been limited thermodynamic research on zirconates. Therefore, we calculated the specific heat of the $(\text{Gd}_x\text{Yb}_{1-x})_2\text{Zr}_2\text{O}_7$ system and explored its relationship with point defects.

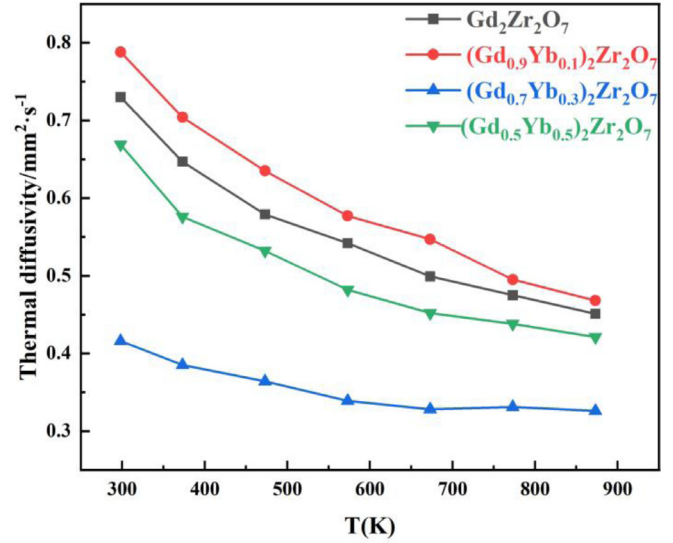


Fig. 8. Thermal diffusion coefficient of $(\text{Gd}_x\text{Yb}_{1-x})_2\text{Zr}_2\text{O}_7$.

As illustrated in Figure 9, at the same temperature, the specific heat of the solid solution is higher than that of $\text{Gd}_2\text{Zr}_2\text{O}_7$, with the lowest value occurring at $\text{Gd}_2\text{Zr}_2\text{O}_7$. The specific heat results, derived from the Neumann-Kopp law, suggest that the specific heat is influenced by contributions from the structure, atomic interactions, and electronic heat capacity [25]. In the $(\text{Gd}_x\text{Yb}_{1-x})_2\text{Zr}_2\text{O}_7$ system, the elevated specific heat of the solid solution is likely due to the lattice distortion around point defects, which enhances the anharmonicity of lattice vibrations.

From the calculation of the phonon mean free path, the phonon mean free path in the $(\text{Gd}_x\text{Yb}_{1-x})_2\text{Zr}_2\text{O}_7$ system is relatively short and smaller than the lattice parameter, indicating significant phonon scattering within the lattice. For insulators, the phonon mean free path at a specific temperature T and for a particular frequency can be expressed as:

$$\frac{1}{\lambda(\omega, T)} = \frac{1}{\lambda_i(\omega, T)} + \frac{1}{\lambda_p(\omega, T)} + \frac{1}{\lambda_b} \quad (9)$$

where λ_i , λ_p , and λ_b are the phonon-free ranges corresponding to interphone scattering, point defect scattering, and grain boundary scattering, respectively [26].

The results indicate that the grain boundary size is significantly larger than the phonon mean free path, meaning that the contribution of grain boundary scattering to the phonon mean free path can be neglected. In this system, the phonon mean free path is predominantly governed by phonon-phonon scattering and defect scattering. Phonon-phonon scattering serves as the primary source of intrinsic thermal resistance in the material, largely arising from the anharmonicity of lattice vibrations.

As shown in Figure 10, in the temperature range from 300 K to 900 K, the thermal conductivity of the materials exhibits a pronounced temperature dependence. The thermal conductivity of $\text{Gd}_2\text{Zr}_2\text{O}_7$, $(\text{Gd}_{0.9}\text{Yb}_{0.1})_2\text{Zr}_2\text{O}_7$, and $(\text{Gd}_{0.5}\text{Yb}_{0.5})_2\text{Zr}_2\text{O}_7$ decreases sharply with increasing temperature. With increasing Yb content, the thermal

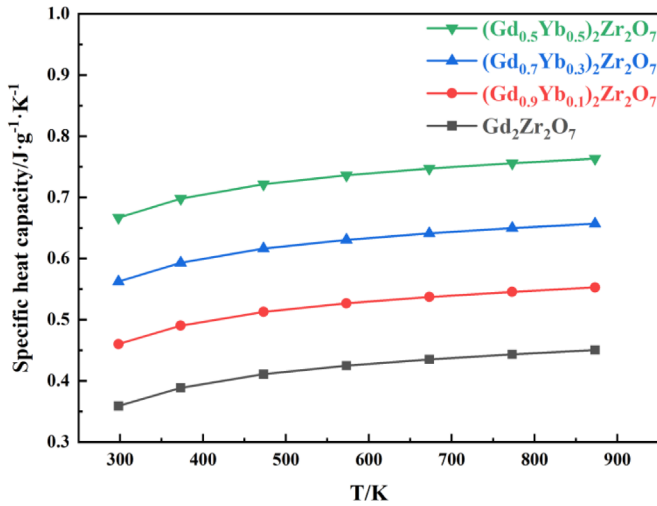


Fig. 9. Specific heat of $(\text{Gd}_x\text{Yb}_{1-x})_2\text{Zr}_2\text{O}_7$.

conductivity initially rises and then decreases, reaching its peak value at $(\text{Gd}_{0.9}\text{Yb}_{0.1})_2\text{Zr}_2\text{O}_7$. In contrast to other studies, where the thermal conductivity of the $(\text{Gd}_x\text{Yb}_{1-x})_2\text{Zr}_2\text{O}_7$ system typically shows a symmetric variation with composition, reaching its minimum at the equimolar ratio ($x=0.5$), our study reveals an asymmetric trend. This asymmetry is due to the relatively limited solubility in the system, preventing the formation of an infinite solid solution.

Regarding the change in thermal conductivity of $(\text{Gd}_{0.7}\text{Yb}_{0.3})_2\text{Zr}_2\text{O}_7$ between 500K and 800K, although the changes in thermal diffusivity and specific heat capacity are monotonic, the thermal conductivity is also affected by other factors. As the temperature rises, the lattice vibration within the material intensifies, and the phonon-phonon scattering is enhanced. This, to a certain extent, offsets the influence of the changes in thermal diffusivity and specific heat capacity on the thermal conductivity, resulting in the fact that the change trend of thermal conductivity does not have a simple linear relationship with that of thermal diffusivity and specific heat capacity. In addition, the increase in temperature may cause slight changes in the microstructure of the material, such as a small amount of dissolution or redistribution of the second phase, which will also have an impact on the thermal conductivity.

As shown in the figure, due to the scattering effects of point defects on phonons, the thermal conductivity of $(\text{Gd}_{0.7}\text{Yb}_{0.3})_2\text{Zr}_2\text{O}_7$ and $(\text{Gd}_{0.5}\text{Yb}_{0.5})_2\text{Zr}_2\text{O}_7$ is lower than that of the matrix material. However, after introducing the same concentration of point defects, the thermal conductivity of $(\text{Gd}_{0.7}\text{Yb}_{0.3})_2\text{Zr}_2\text{O}_7$ decreases to a greater extent than that of $(\text{Gd}_{0.5}\text{Yb}_{0.5})_2\text{Zr}_2\text{O}_7$. This is partly because the intrinsic phonon scattering in $(\text{Gd}_{0.7}\text{Yb}_{0.3})_2\text{Zr}_2\text{O}_7$ is weaker than in $(\text{Gd}_{0.5}\text{Yb}_{0.5})_2\text{Zr}_2\text{O}_7$, resulting in a more significant reduction in thermal conductivity after the introduction of point defects. Additionally, this phenomenon is also influenced by the concentration of point defects and the structural changes they induce. Doping Yb^{3+} ions with smaller radii into $(\text{Gd}_{0.7}\text{Yb}_{0.3})_2\text{Zr}_2\text{O}_7$ reduces the cation radius ratio between the A and B sites of the fluorite

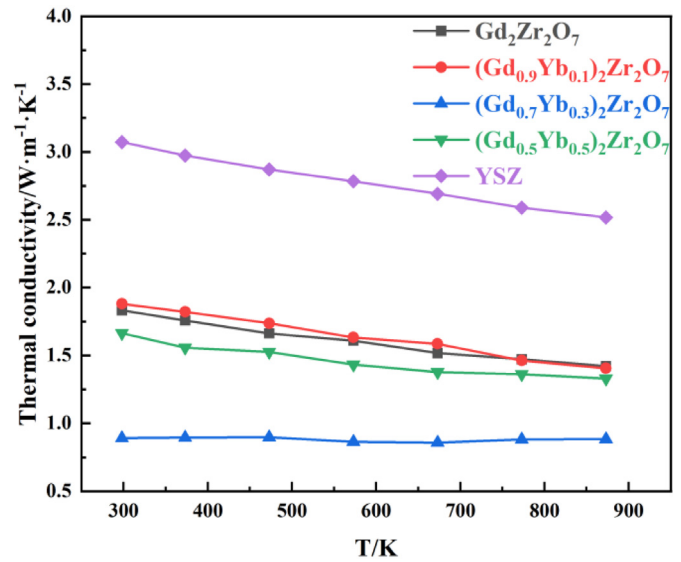


Fig. 10. Thermal conductivity of $(\text{Gd}_x\text{Yb}_{1-x})_2\text{Zr}_2\text{O}_7$.

structure, causing structural disorder and a decrease in lattice energy. This, in turn, increases the anharmonicity of the lattice, leading to enhanced phonon scattering.

From Figure 10, it can be seen that, within the temperature range of 298 K to 873 K, the thermal conductivity of $\text{Gd}_2\text{Zr}_2\text{O}_7$, $(\text{Gd}_{0.9}\text{Yb}_{0.1})_2\text{Zr}_2\text{O}_7$, $(\text{Gd}_{0.7}\text{Yb}_{0.3})_2\text{Zr}_2\text{O}_7$, and $(\text{Gd}_{0.5}\text{Yb}_{0.5})_2\text{Zr}_2\text{O}_7$ is lower than that of YSZ. Among these materials, $(\text{Gd}_{0.7}\text{Yb}_{0.3})_2\text{Zr}_2\text{O}_7$ exhibits the lowest thermal conductivity, with a minimum value of $0.858 \text{ W}\cdot\text{m}^{-1}\cdot\text{K}^{-1}$ at 675 K. Compared to the traditional thermal barrier coating material YSZ, it demonstrates superior thermal insulation properties, effectively reducing heat transfer and providing better protection to the turbine substrate material in geothermal power generation equipment from high-temperature degradation.

4 Conclusion

Structural advantages: The $(\text{Gd}_x\text{Yb}_{1-x})_2\text{Zr}_2\text{O}_7$ ceramics ($x=0.5, 0.7, 0.9, 1$) synthesized by solid-state reaction exhibit a fluorite-type structure and demonstrate good phase stability from room temperature to 873 K.

Mechanical improvement: Yb^{3+} doping reduces the thermal conductivity of $(\text{Gd}_x\text{Yb}_{1-x})_2\text{Zr}_2\text{O}_7$ ceramics. At $x=0.7$, the thermal conductivity reaches its lowest value of $0.858 \text{ W}\cdot\text{m}^{-1}\cdot\text{K}^{-1}$ at 675 K. Based on the A-site ion radius ratio ($r_{\text{Gd}^{3+}} = 0.938 \text{ \AA}$, $r_{\text{Yb}^{3+}} = 0.86 \text{ \AA}$), when $x=0.7$, the average ion radius (0.886 \AA) is 1.23 times closer to Zr^{4+} (0.72 \AA), meeting the radius ratio threshold (1.46–1.78) for fluorite structure stability. This ratio can serve as a theoretical design reference.

With increasing Yb^{3+} doping, both the hardness and fracture toughness of $(\text{Gd}_x\text{Yb}_{1-x})_2\text{Zr}_2\text{O}_7$ ceramics improve. The Young's modulus first increases and then decreases, which results in an overall enhancement of their mechanical properties.

The reduction in thermal conductivity is primarily attributed to the shrinkage of the unit cell volume caused by Yb^{3+} doping.

The composition with $x = 0.7$ is proposed as a candidate material for thermal barrier coatings on geothermal turbine blades, owing to its minimum thermal conductivity ($0.858 \text{ W}\cdot\text{m}^{-1}\cdot\text{K}^{-1}$ at 675 K) and sufficient mechanical strength (hardness 9.2 GPa, fracture toughness $2.1 \text{ MPa}\cdot\text{m}^{1/2}$). This study did not investigate the thermal expansion properties above 873 K, and the high-temperature oxidation resistance of $(\text{Gd}_{0.7}\text{Yb}_{0.3})_2\text{Zr}_2\text{O}_7$ requires further optimization. Future work may combine nanocomposite technologies to enhance stability at elevated temperatures. Future studies will include direct CTE measurements (300–1500 K) to fully assess thermal compatibility with turbine substrates (e.g., Inconel 718).

Funding

Not applicable.

Conflicts of interest

The author states no conflict of interest.

Author contribution statement

Wenxin Guo contributes to methodology, analysis, data collection, draft preparation, manuscript editing.

Data availability statement

Data will be made available on reasonable request.

References

1. Y.H. Lü, Z.J. Wu, J.X. Tang et al., Study on thermal insulation behavior of nano-YSZ thermal barrier coatings, *Chin. J. Surf. Eng.* **19** (2006) 24–27
2. Z.H. Zhou, P.D. Ding, B. Chen et al., Effect of phase content variation on the properties of zirconia ceramics, *J. Metal Heat Treat.* **27** (2002) 43–45+75
3. G.W. Goward, Progress in coatings for gas turbine airfoils, *Surf. Coatings Technol.* **108** (1998) 73
4. H.B. Guo, S.K. Gong, H.B. Xu, Research progress on thermal barrier coating technology for advanced aircraft engines, *Prog. Mater. Sci.* **28** (2009) 18–26
5. X.H. Yuan, H.B. Guo, H. Peng et al., High-temperature thermophysical properties of $\text{Gd}_2\text{Zr}_2\text{O}_7$ ceramics and preparation of $\text{Gd}_2\text{Zr}_2\text{O}_7$ -8YSZ dual coatings, *J. Adv. Mater.* **2011** (2011) 18–24
6. Q. Chen, J. Xu, H. Wang et al., Thermophysical properties of Yb^{3+} -doped nonstoichiometric gadolinium zirconate ceramics, *Ceram. Int.* **50** (2024) 47813–47823
7. A. Saha, K. Kumari, B.S. Deb et al., Inductively coupled plasma optical emission spectroscopic determination of trace rare earth elements in highly refractory gadolinium zirconate ($\text{Gd}_2\text{Zr}_2\text{O}_7$), *RSC Adv.* **14** (2024) 31422–31428
8. Q. Chen, H. Wang, J. Wu et al., Effect of Yb^{3+} on the thermophysical and mechanical properties of gadolinium zirconate ceramics: first-principles calculations and experimental study, *J. Alloys Compd.* **100717** (2024) Article ID 6480
9. X.P. Zhang, X.G. Chen, H.S. Zhang, Research progress on ceramic materials for thermal barrier coatings, *J. Artif. Cryst.* **43** (2014) 45–50
10. Practical thermodynamic data handbook of inorganic compounds, *Nonferrous Metals* **1980** (1980) 45
11. Q. Wu, X. Zhang, H.R. Peng et al., Thermophysical properties of pyrochlore structure $\text{A}_2\text{B}_2\text{O}_7$ thermal barrier coating materials: a review, *Therm. Spray Technol.* **23** (2014) 1
12. B.P. Mandal, A.K. Tyagi, Preparation and high temperature-XRD studies on a pyrochlore series with the general composition $\text{Gd}_{2-x}\text{Nd}_x\text{Zr}_2\text{O}_7$, *J. Alloys Compd.* **437** (2007) 260
13. X.L. Xia, Study on the ordered-disordered transition and electrical properties of cation-doped rare earth zirconates, Harbin Institute of Technology, 2011
14. C.L. Wan, Z.X. Qu, A.B. Du et al., Influence of B site substituent Ti on the structure and thermophysical properties of $\text{A}_2\text{B}_2\text{O}_7$ -type pyrochlore $\text{Gd}_2\text{Zr}_2\text{O}_7$, *Acta Mater.* **57** (2009) 4782
15. Y.H. Zhang, M. Xie, F. Zhou et al., Low thermal conductivity in $\text{La}_2\text{Zr}_2\text{O}_7$ pyrochlore with A-site partially substituted with equimolar Yb_2O_3 and Er_2O_3 , *Ceram. Int.* **40** (2014) 9151
16. M.A. Subramanian, G. Aravamudan, R.G.V. Subba, Oxide pyrochlores—A review, *Prog. Solid State Chem.* **15** (1983) 55
17. N. Hanako, H. Yamamura, T. Aarai et al., Effect of cation radius ratio and unit cell free volume on oxide-ion conductivity in oxide systems with pyrochlore-type composition, *J. Ceram. Soc. Jpn.* **112** (2004) 541
18. F. Huang, Study on grain refinement and shape memory effect of Cu-Zn-Al alloys, Wuhan University of Technology, 2006
19. Z.G. Liu, Study on the microstructure and physical properties of $\text{A}_2\text{Zr}_2\text{O}_7$ -type rare earth zirconate materials, Harbin Institute of Technology, 2009
20. Z.X. Qu, Defect chemistry and thermophysical properties of rare earth oxide thermal barrier ceramic materials, Tsinghua University, 2009
21. M. Zhao, Effect of doping on the thermophysical properties of zirconia-based thermal barrier coating materials, Tsinghua University, 2016
22. J. Wu, H. Wang, J. Xu et al., Enhanced thermophysical and mechanical properties of gadolinium zirconate ceramics via non-stoichiometric design, *J. Eur. Ceram. Soc.* **44** (2024) 116790
23. H.X. Zhao, C.M. Deng, L. Fu et al., Research progress on gadolinium zirconate materials for thermal barrier coatings, *Surf. Technol.* **51** (2022) 116–128
24. L. Fu, J. Mao, Z.Q. Deng et al., Research progress on the ceramic topcoat of gadolinium zirconate thermal barrier coatings, *Aerosp. Manuf. Technol.* **64** (2021) 77–87
25. Z.D. Guan, Z.T. Zhang, J.S. Jiao, Physical properties of inorganic materials, Tsinghua University Press, Beijing, 2008
26. L. Fu, J. Mao, Z.Q. Deng et al., Study on preparation and properties of gadolinium zirconate thermal barrier coatings by PS-PVD, *Surf. Technol.* **50** (2021) 293–300

Cite this article as: Wenxin Guo, Study of the physical properties of Yb_2O_3 -doped $\text{Gd}_2\text{Zr}_2\text{O}_7$ ceramics as a thermal barrier coating material, *Manufacturing Rev.* **12**, 26 (2025), <https://doi.org/10.1051/mfreview/2025023>